Corrosion of Pure Magnesium and Binary Magnesium Alloy in Ringer's Solution

A. Fijołek iD

AGH University of Krakow, Faculty of Foundry Engineering
Reymonta 23 Str., 30-059 Krakow, Poland
Corresponding author. E-mail address: afijolek@agh.edu.pl

Abstract

The work presents monitoring of the corrosion rate for pure magnesium and the binary magnesium alloy $Mg_{72}Zn_{28}$. Alloying elements with a purity of 99.9% were used. The melting was performed under the protection of inert gas - argon in an induction furnace. The liquid alloy was poured into a copper mold. In order to make amorphous ribbons, the obtained samples in the form of rods were re-melted on a melt spinner machine. The next step was to perform corrosion tests in Ringer's solution. Corrosion tests were carried out at a temperature of 37°C and pH 7.2. The purpose of using Ringer's solution was to recreate the conditions for the body fluids of the human body. The use of the following research methods, such as: OCP (open circuit potential), LSV (linear sweep voltammetry) and EIS (electrochemical impedance spectroscopy), was aimed at determining the corrosion resistance of the tested materials. Tests carried out in Ringer's solution showed that pure magnesium has significantly worse corrosion resistance than the binary $Mg_{72}Zn_{28}$ alloy. The conducted research also confirmed that the cathodic reaction takes place faster on the surface of amorphous ribbons. It was also confirmed that for both crystalline materials there is diffusion of chloride ions through the corrosion product layer. SEM-EDS tests were performed on the surface of an amorphous ribbon of the $Mg_{72}Zn_{28}$ alloy after corrosion in Ringer's solution.

Keywords: Biodegradability, Corrosion, Ringer solution, Mg-Zn alloy, Equivalent circuit

1. Introduction

Magnesium alloys are used in medicine as biodegradable materials [1]. Magnesium as a pure component undergoes corrosion, therefore an alloying additive in the form of zinc is introduced [2]. The introduction of zinc results in improved corrosion resistance, while the addition of calcium accelerates the wound healing process and is a building block of human bone [3, 4]. The Young's modulus for magnesium is 41–45 GPa, a parameter similar to that of human bone, which has a Young's modulus of 3–20 GPa. This parameter is definitely more favorable in relation to the transfer of stresses in relation to materials such as stainless steel, whose Young's modulus is 189–205 GPa, and Ti alloys, whose Young's modulus is 110–117 GPa [3, 5].

In addition, these ingredients are compatible with the human body, where they occur naturally [6]. Moreover, Mg alloys do not negatively affect imaging using magnetic resonance imaging and computed tomography, which also makes them suitable for use in the biomedical field as biodegradable implants [3]. Implants made of magnesium alloys with the addition of zinc are slowly biodegradable in the human body and do not cause allergic reactions and are not toxic to the human body [7]. Monitoring the corrosion resistance for biodegradable magnesium alloys is extremely important due to the area of their application [8]. These materials must have adequate corrosion resistance so that the applied part does not degrade too early during the healing process of the damaged tissue or bone [9].

In their previous work, scientists conducted tests on samples of three-component magnesium, calcium and zinc alloys [4].

The paper presents test results for the MgZnCa and ZnMgCa alloy. The tests were carried out for both crystalline and amorphous alloys. The results of corrosion tests showed that ribbons with an amorphous structure are characterized by better corrosion resistance compared to samples with a crystalline structure Kubásek and Vojtěch [10] also conducted corrosion tests on two-component MgZn alloys with a crystalline structure in a physiological solution (9 g/l NaCl). In the paper [9], the presented conclusions show that the addition of zinc in the content (1 and 3 wt.%) improves the corrosion resistance of a two-component magnesium-based alloy. In other works, scientists point out that the corrosion of magnesium is largely influenced by alloy additions in solid solution [11–14]. However, the solubility of the alloying elements in crystalline magnesium is limited, which means that the corrosion mechanisms can be modified, but not completely changed [11]. In the work [11] scientists draw attention to the evolution of hydrogen, which remains a problem during the corrosion of crystalline magnesium alloys. In the work [15] scientists show that a larger range of alloying elements in the amorphous single-phase structure allows the production of specific metallic glasses with significantly improved corrosion properties. This means that there may be metallic glasses of magnesium alloys in which the evolution of hydrogen during progressive corrosion is significantly reduced or even completely prevented [11]. Moreover, since there is no dislocation-based plastic deformation mechanism in amorphous alloys, bulk metallic glasses [16–19] show much better strength and flexibility parameters. In the work [20] six unique Ca-based metallic glasses were developed. Metallic glasses are designed to consist exclusively of the biocompatible elements Ca, Mg and Zn for their potential use as bioresorbable metals in the orthopaedic field [20]. In vitro biocorrosion studies using a combination of polarization and mass loss techniques have shown that the corrosion rate of these alloys is relatively high and, in some cases, can be controlled depending on the chemical composition of the alloy being tested [20].

In previous publications, the authors [21–23] developed tests in which, based on the selected GFA parameters, an amorphous structure was obtained for samples with a diameter of 2 to 11 mm, while the authors of the paper [24] obtained a diameter of 14 mm for the amorphous structure using the GFA parameters for the $Mg_{65}Cu_{7.5}Ni_{7.5}Ag_5Zn_5Gd_5Y_5$ alloy. The thermoplastic forming window (TPF) of magnesium alloy-based BMG is very small. GFA can only be achieved at temperatures above the glass transition and below the first crystallization. The small TPF window and low critical thickness constitute a limitation in the production of Mg-based BMGs. Therefore, BMGs based on a magnesium alloy can be used for thin elements.

Based on the literature analysis, the influence of the crystalline and amorphous structure on the corrosion properties of the two-component $Mg_{72}Zn_{28}$ alloy in Ringer's solution was analyzed. The results of these tests were compared to pure magnesium.

2. Materials and specimen preparation

The alloy additives used to obtain the $Mg_{72}Zn_{28}$ alloy had a purity of 99.9%. Melting was carried out in an induction furnace using inert gas - argon. The liquid casting alloy was poured into a metal copper mold to obtain cylindrical samples with a diameter of 20 mm and a height of 50 mm. The samples were then mechanically processed and their final dimensions were 10 mm in diameter and 50 mm in height. The obtained cylindrical samples were re-melted on a melt spinner, which resulted in obtaining amorphous ribbons with an average thickness of 100 to 150 μm. The wheel rotation speed of the melt spinner machine used was 35 m/min. Figure 1 shows a diagram of a melt spinner device for producing metallic materials with an amorphous structure.
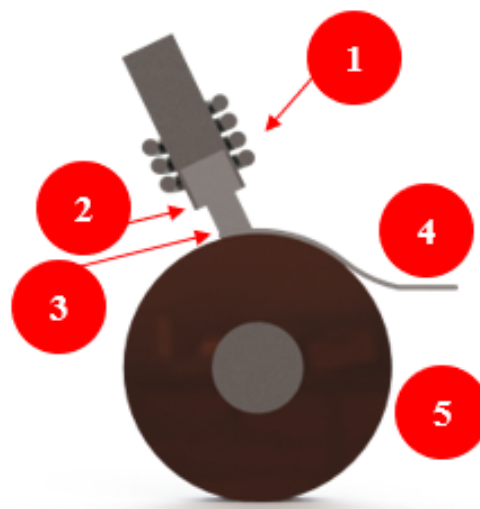

Fig. 1. Scheme of the construction of the 'melt spinner' device for the production of metallic materials with an amorphous structure: 1 – induction coil, 2 – head, 3 – liquid material, 4 – ribbon, 5 – copper drum

Corrosion tests were carried out in Ringer's solution simulating human body fluids under the following conditions - temperature 37°C and pH 7.2. The following components were used to prepare Ringer's solution: NaCl 8.6 (g/dm³), KCl 0.3 (g/dm³) and $CaCl_2$ anhydrous 0.25 (g/dm³). The obtained crystalline samples for pure magnesium and the binary $Mg_{72}Zn_{28}$ alloy were polished on abrasive papers from grit 1200 to 4000 before corrosion tests. After each polishing stage, the samples were rinsed in ethanol for 5 minutes in ultrasound. In order to determine the corrosion resistance of the $Mg_{72}Zn_{28}$ alloy and pure magnesium, polarization curves (LSV—linear sweep voltammetry) were prepared. The potential scanning rate was 1 mV/s. Measurements were carried out in aerated Ringer's solution at a temperature of 37°C and pH 7.2. The spectra in the EIS technique used were measured at OCP, where the amplitude of the interfering signal was 10 mV and the frequency range was from 100 kHz to 0.03 Hz. ZView software was used to adjust the electrical equivalent circuit. The matching was made on the basis of obtained experimental EIS spectra of the $Mg_{72}Zn_{28}$ alloy immersed in Ringer's solution at a temperature of 37°C and pH 7.2. After 1800 seconds, a steady state was obtained for the sample immersed in Ringer's solution and measurements of EIS spectra were started for both crystalline samples (before the melt

spinning process) and amorphous ribbons (after the melt spinning process). An AUTOLAB PGSTAT 128 potentiostat was used to perform the measurements. The scheme of the station where corrosion tests carried out is shown in Figure 2.
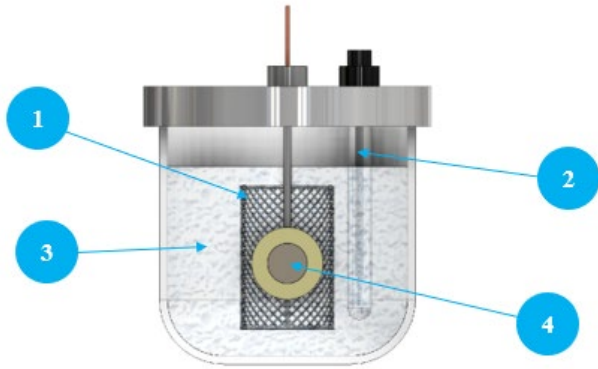

Fig. 2. Scheme of the stand used for corrosion tests: 1 – counter electrode (sectional view), 2 – reference electrode, 3 – electrolyte (Ringer's solution), 4 – tested material sample (working electrode), which is surrounded by a platinum mesh (counter electrode)

SEM tests were performed on TESCAN MIRA GMU and EDS tests were performed on AZtec Live Advanced from Oxford Instruments.

3. Results

The results of XRD tests of a sample cast from the $Mg_{72}Zn_{28}$ alloy into a steel mould (marked as crystalline) are shown in Figure 3. The structure of the sample marked as starting sample has a crystalline structure. The presence of two phases can be observed, i.e. a-Mg and $Mg_{102.08}Zn_{39.6}$. However, the XRD pattern of the ribbon cast also from the $Mg_{72}Zn_{28}$ alloy using the melt spinning method is shown in Figure 4. The ribbon showed an amorphous structure.
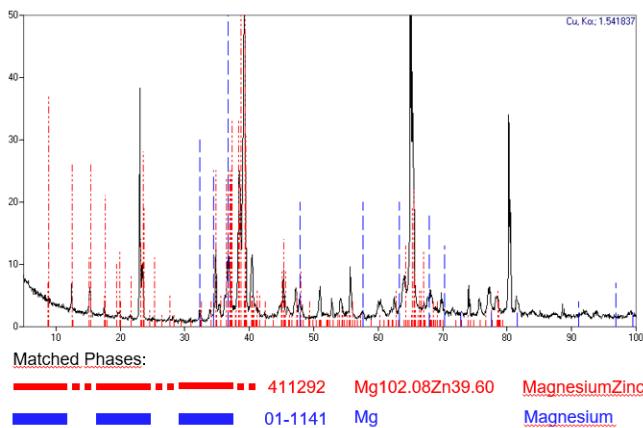

Fig. 3. X-ray diffraction results for $Mg_{72}Zn_{28}$ crystalline sample (before melt spinning process)
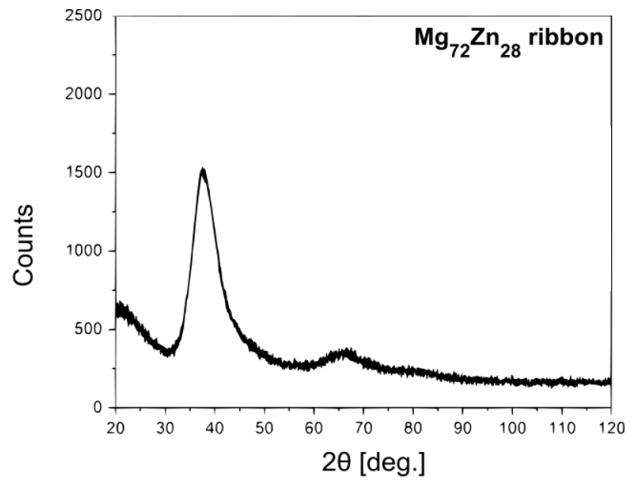

Fig. 4. X-ray diffraction results for $Mg_{72}Zn_{28}$ amorphous sample (after melt spinning process)

To determine the corrosion resistance of Mg and $Mg_{72}Zn_{28}$ alloy, the dynamic polarisation curves were performed in the Ringer's solution, Figure 5. The pure Mg and magnesium alloys exhibit the active corrosion. In the anodic branch, the sharp increase in the current density is observed. The increase in the anodic current density is related with the dissolution of magnesium according with the reaction (1).

$$Mg \rightarrow Mg^{2+} + 2e^- \qquad (1)$$

Electrons released in the anodic dissolution of magnesium are consumed in the reduction reaction of water, and hydroxy ions are formed, reaction (2).

$$2H_2O + 2e^- \rightarrow H_2 + 2OH^- \qquad (2)$$

Magnesium ions react with the hydroxyl ions and magnesium hydroxide $Mg(OH)_2$ is formed as a corrosion main product. It should be noticed that the highest values of cathodic current density are measured for $Mg_{72}Zn_{28}$ amorphous specimen, red curve in Figure 5. In contrast, the lowest values of current density in the cathodic region were measured for pure magnesium, the green dashed curve in Figure 5. Compare to the pure Mg, higher current density in the cathodic domain was obtained for the crystalline specimen, blue curve Figure 5, The highest values of the current density in the cathodic branch were measured for amorphous specimen $Mg_{72}Zn_{28}$, red curve in Figure 5. This result indicates that the water reduction reaction occurs preferentially on the surface of amorphous alloy $Mg_{72}Zn_{28}$ alloy. The formation of OH$^-$ ions causes the alkalization of the alloy surface, and $Mg(OH)_2$ is formed. This leads to a shift of the polarization curves toward higher potential values, red curve Figure 5. In the anodic domain the current density slowly increases with increasing of potential values for pure Mg and for crystalline $Mg_{72}Zn_{28}$ alloy, green dashed and blue curves Figure 5. However, for the amorphous $Mg_{72}Zn_{28}$ sample (red curve), the current plateau is visible in the potential range between -1.30 V and -1.20 V. The current density measured at the potential -1.25 V is 0.083 mA/cm^2, 0.123 mA/cm^2 and

0.321 mA/cm² for amorphous Mg$_{72}$Zn$_{28}$ alloy, crystalline Mg$_{72}$Zn$_{28}$ alloy and pure Mg, respectively.
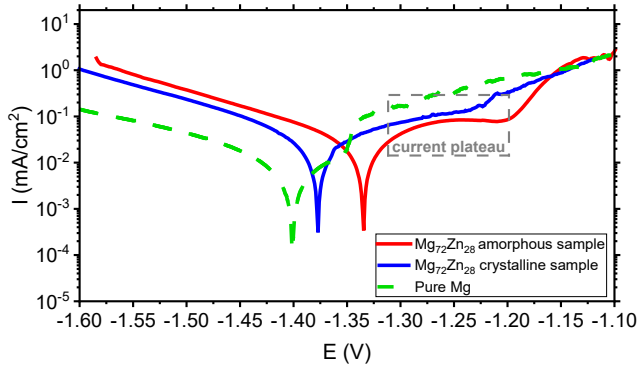

Fig. 5. Polarization curves performed for Mg$_{72}$Zn$_{28}$ and pure Mg alloys in Ringer's solution at 37°C, pH 7.2

The course of polarization curves indicates that the amorphous Mg$_{72}$Zn$_{28}$ alloy sample is more resistant to corrosion than the crystalline sample. The values of anodic current density in the passive range are lower compared to crystalline Mg$_{72}$Zn$_{28}$ alloy and pure Mg, Figure 5.

As shown in Figure 6, the corrosion potential for the crystalline alloy gradually increases and after 1800 seconds of immersion in Ringer's solution it reaches a value of -1370 mV (blue curve). After immersing the amorphous alloy in the electrolyte solution, the corrosion potential initially decreases and then increases, reaching a value of -1335 mV after 1800 seconds of immersion (red curve, Figure 6). The increase in corrosion potential when the alloys are immersed in Ringer's solution indicates the formation and growth of a passive layer. The difference in corrosion potential between the amorphous and crystalline samples is 35 mV. A higher value of the corrosion potential for an amorphous sample suggests that the passive layer growing on its surface is more stable, which increases its corrosion resistance.
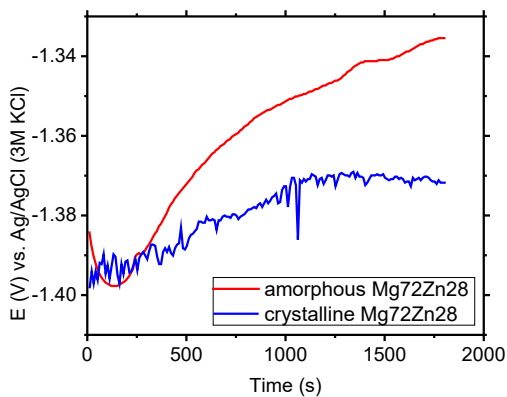

Fig. 6. Evolution of the open circuit potential versus time of crystalline Mg$_{72}$Zn$_{28}$ alloy (blue curve) and amorphous Mg$_{72}$Zn$_{28}$ alloy (red curve)
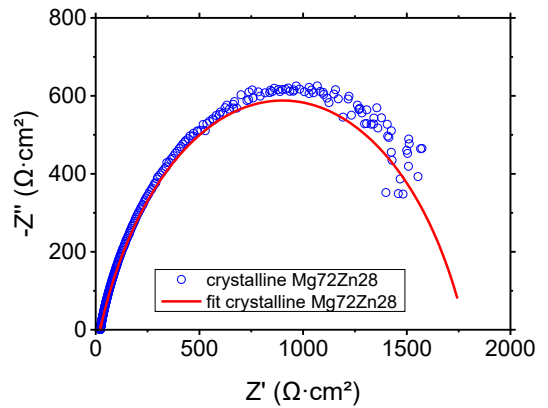

Fig. 7. Nyquist diagram with respective fitting line for Mg$_{72}$Zn$_{28}$ alloy crystalline sample of immersion at open circuit potential in Ringer's solution at 37°C
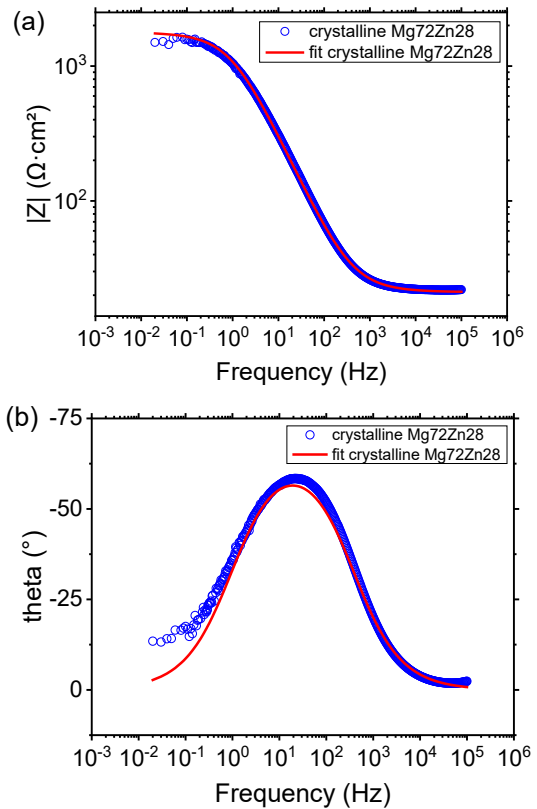

Fig. 8. Bode diagrams (a, b) with respective fitting line for Mg$_{72}$Zn$_{28}$ alloy crystalline sample of immersion at open circuit potential in Ringer's solution at 37°C

Figures 7 and 8 show the EIS spectra obtained for crystalline sample of Mg$_{72}$Zn$_{28}$ alloy in the Ringer's solution. Figure 7 presents the Nyquist diagram and Figure 8 presents the Bode diagram, respectively. EIS spectrum shows one capacitive loop. For fitting the experimental data, the electrical equivalent circuit presented in Figure 9 was used. This electrical circuit consists of 3 elements: R1, CPE and R2.

The constant phase element CPE is define with the following equation (3) [4, 25]:

$$\hat{Z}_{CPE} = \frac{1}{Z(j\omega)^n} \qquad (3)$$

where:

CPE-T – the capacitance parameter in $F \cdot cm^{-2} \cdot s^{\phi-1}$ which depends on the electrode potential,

n – is related to the angle of rotation of purely capacitive line on the complex plane plots:

$\alpha = 90°(1 - \phi)$. When $n = 1$, the purely capacitive behavior of electrode is obtained. Equation (3) represents pure capacitance for $n = 1$, infinite Warburg impedance for $n = 0.5$, pure resistance for $n = 0$, and pure inductance for $n = -1$, respectively.
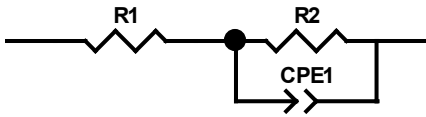

Fig. 9. The equivalent circuit used for fitting experimental EIS $Mg_{72}Zn_{28}$ alloy crystalline sample immersed in Ringer`s solution at 37°C

In equivalent circuits (Figure 9), R1 is the electrolyte resistance, and R2 and CPE1 are the resistance and capacitive reactance resulting from charge transfer, respectively. R2 directly indicates the anticorrosion ability, and CPE1 can be used to evaluate the degree of penetration of the electrolyte into the surface layer, which is related to the thickness, density, and defect structure of the layer [26]. The fitting parameters for the developed equivalent circuit shown in Figure 9 are presented in Table 1.

Table 1.
Fitting parameters obtained from the EIS measurements of $Mg_{72}Zn_{28}$ alloy crystalline sample alloy immersed in Ringer's solution at 37°C. For fitting the equivalent circuit presented in Figure 9 was used.

Element	R1 ($\Omega \cdot cm^2$)	CPE1-T ($F \cdot cm^{-2} \cdot s^{\phi-1}$)	CPE1-n ($F \cdot cm^{-2} \cdot s^{\phi-1}$)	R2 ($\Omega \cdot cm^2$)
Value	21.09	0.00014335	0.75	1761
Error	0.063	1.0939E-06	0.0014	9.2
Error (%)	0.30	0.80	0.19	0.52

The value CPE1-n equal 0.75 indicates that the corrosion layer formed on the surface of $Mg_{72}Zn_{28}$ crystalline alloy exhibit rather capacitive behaviour.

Figures 10-11 show the EIS spectra obtained for the amorphous sample of $Mg_{72}Zn_{28}$ alloy in the Ringer solution. The EIS spectrum shows two capacitive loops, one visible at the high frequency range and the second at the low frequency range, respectively.
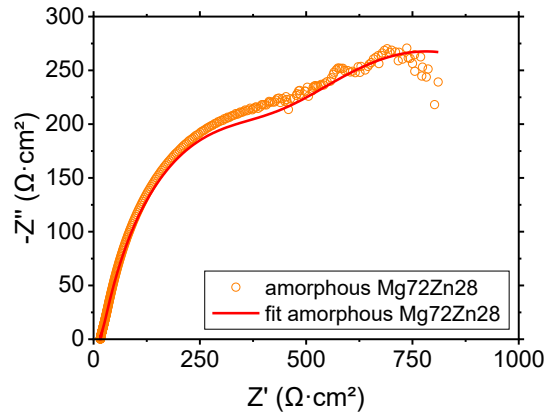

Fig. 10. Nyquist diagram with respective fitting line for $Mg_{72}Zn_{28}$ alloy amorphous sample of immersion at open circuit potential in Ringer`s solution at 37°C
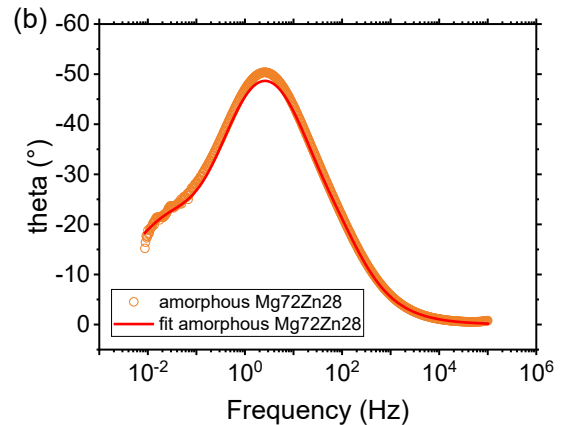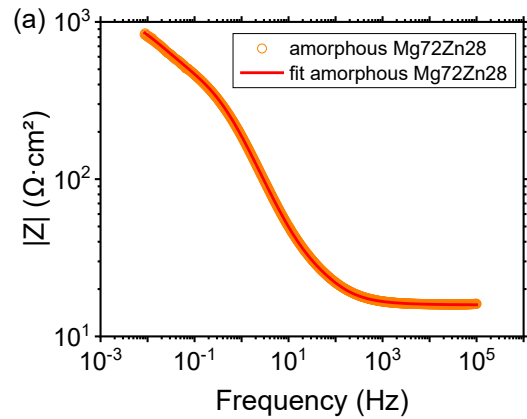

Fig. 11. Bode diagrams (a, b) with respective fitting line for $Mg_{72}Zn_{28}$ alloy amorphous sample of immersion at open circuit potential in Ringer`s solution at 37°C

The experimental EIS spectra obtained for amorphous specimen were fitted by means of electrical equivalent circuit presented in Figure 12. The circuit for this alloy consists of the following elements: R1—solution resistance, R2—change transfer resistance and R3—resistance of the surface layer, CPE1—constant phase element related to the double layer capacity,

CPE2—constant phase element related to the surface layer formed at the surface of amorphous Mg$_{72}$Zn$_{28}$ alloy.
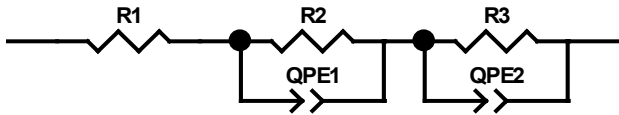

Fig. 12. The equivalent circuit used for fitting experimental EIS Mg$_{72}$Zn$_{28}$ alloy amorphous sample immersed in Ringer`s solution at 37°C

The value of phase constant element QPE1-n equal 0.79 confirms the capacitive properties of the passive film formed on the surface of amorphous Mg$_{72}$Zn$_{28}$ alloy, Table 2. However, the presence of high concentration of Cl$^-$ ions in the Ringer solution cause damage of the passive layer, dissolution of the metallic matrix, formation of the corrosion products mainly magnesium oxide and hydroxide. The QPE2-n value equal 0.55 confirms that the diffusion of Cl$^-$ ions through the hydroxides layer can take place. The fitting parameters for the developed equivalent circuit shown in Figure 12 are presented in Table 2 for amorphous sample of Mg$_{72}$Zn$_{28}$ alloy.

Table 2.
Fitting parameters obtained from the EIS measurements of Mg$_{72}$Zn$_{28}$ alloy amorphous sample alloy immersed in Ringer's solution at 37°C

Element	Value	Error	Error (%)
R1 ($\Omega\cdot$cm^2)	15.6	0.015497	0.09934
R2 ($\Omega\cdot$cm^2)	288.5	1.6091	0.55775
QPE1-Q (F$\cdot$cm$^{-2}\cdot$sϕ^{-1})	0.00032577	1.7648E-06	0.54173
QPE1-n (F$\cdot$cm$^{-2}\cdot$sϕ^{-1})	0.79	0.0040641	0.51345
R3 ($\Omega\cdot$cm^2)	1128	8.7057	0.77178
QPE2-Q (F$\cdot$cm$^{-2}\cdot$sϕ^{-1})	6.9145E-5	3.0419E-07	0.43993
QPE2-n (F$\cdot$cm$^{-2}\cdot$sϕ^{-1})	0.55	0.001691	0.30818

EDS scans were performed on the surface of an amorphous ribbon made of the Mg$_{72}$Zn$_{28}$ alloy after corrosion in Ringer's solution. The EDS maps shown in Figure 13 revealed the presence of magnesium, zinc and oxygen. Additionally, corrosion products, consisting mainly of magnesium, zinc and oxygen, are visible on the ribbon surface. The analysis of EDS maps shows that the concentration of magnesium and zinc in the corrosion products is lower than on the ribbon surface, while the opposite is true in the case of oxygen. This analysis is confirmed by the results presented in Figure areas four and five. Area one concerns the ribbon surface without corrosion products and area six concerns the surface of the ribbon with corrosion products. The analysis of the EDS results shows that the corrosion products probably consist mainly of magnesium and zinc oxides.
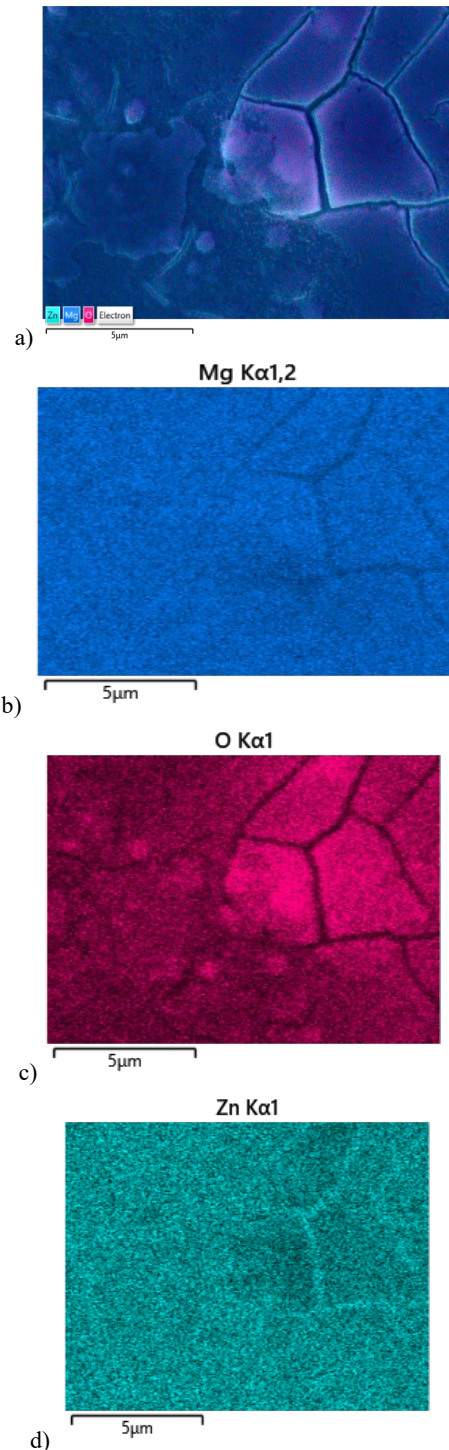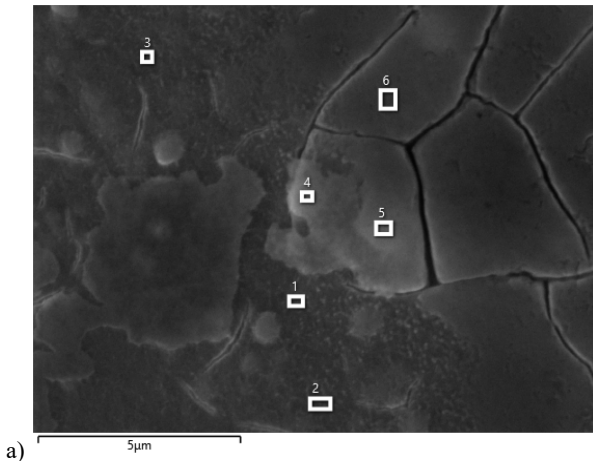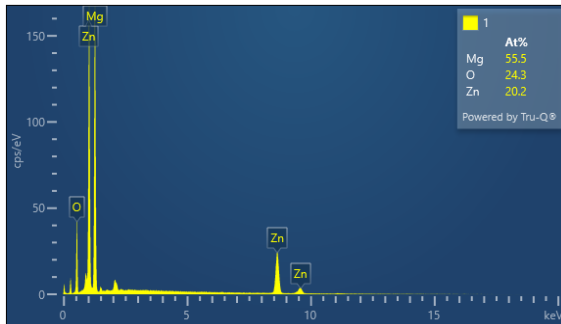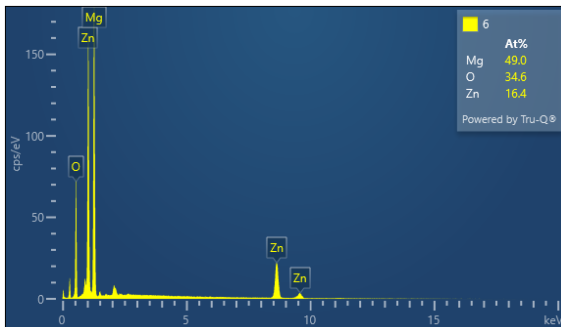

Fig.13. The EDS map EDS map of the surface of an amorphous ribbon made of Mg$_{72}$Zn$_{28}$ alloy after corrosion in Ringer's solution with elemental distribution. (a) EDS map of the distribution of magnesium, zinc and oxygen on the surface of an amorphous ribbon, (b) magnesium distribution, (c) oxygen distribution and (d) zinc distribution

Fig. 14. (a) SEM top-view images of the ribbon made of $Mg_{72}Zn_{28}$ amorphous alloy after corrosion in Ringer's solution. (b-c) Spectrum obtained from EDS analysis for two area one and six, marked in (a)

4. Conclusions

From the experimental results the following conclusions can be drawn:

1) The reduction reactions occur preferentially on the surface of amorphous alloy $Mg_{72}Zn_{28}$ alloy.
2) The lowest value of the current density in the passive range and the increases of the OCP versus time for the amorphous specimen suggests this specimen undergoes the passivation

and its dissolution is slower than the crystalline $Mg_{72}Zn_{28}$ alloy.

3) Dissolution of the amorphous $Mg_{72}Zn_{28}$ alloy consist of two steps: break down the passive film, formation of the corrosion products and diffusion of ions through the corrosion layer.
4) Corrosion products are a mixture of magnesium and zinc oxides.

Acknowledgements

References

[1] Persaud-Sharma, D. & McGoron, A. (2012). Biodegradable Magnesium alloys: a review of material development and applications. *Journal of Biomimetics Biomaterials and Tissue Engineering.* 12, 25-39. https://doi.org/10.4028/www.scientific.net/JBBTE.12.25.

[2] Jarzębska, A., Bieda, M., Kawałko, J, Koprowski, P., Sztwiertnia, K., Pachla, W. & Kulczyk, M. (2018). A new approach to plastic deformation of biodegradable zinc alloy with magnesium and its effect on microstructure and mechanical properties. *Materials Letters.* 211, 58-61. https://doi.org/10.1016/j.matlet.2017.09.090.

[3] Zheng, Y. (2015). *Magnesium alloys as degradable biomaterials*. CRC Press.

[4] Fijołek, A., Lelito, J., Krawiec, H., Ryba, J. & Rogal, Ł. (2020). Corrosion resistance of Mg72Zn24Ca4 and Zn87Mg9Ca4 alloys for application in medicine. *Materials.* 13(16), 3515, 1-15. https://doi.org/10.3390/ma13163515.

[5] Staiger, M.P., Pietak, A.M., Huadmai, J. & Dias, G. (2006). Magnesium and its alloys as orthopedic biomaterials: A review. *Biomaterials.* 27(9), 1728-1734. https://doi.org/10.1016/j.biomaterials.2005.10.003.

[6] Song, G.L. (2011). *Corrosion of Magnesium Alloys*. Elsevier.

[7] Makar, G.L. & Kruger, J. (1993). Corrosion of magnesium. *International Materials Reviews.* 38(3), 138-153. https://doi.org/10.1179/imr.1993.38.3.138.

[8] Zreiqat, H., Howlett, C.R. Zannettino A, Evans, P., Schulze-Tanzil, G., Knabe, C. & Shakibaei, M. (2002). Mechanisms of magnesium-stimulated adhesion of osteoblastic cells to commonly used orthopaedic implants. *Journal Biomedical Materials Research.* 62(2), 175-184. https://doi.org/10.1002/jbm.10270.

[9] Gali, E. (2011). Activity and passivity of magnesium (Mg) and its alloys. *Corrosion of Magnesium Alloys.* 66-114. https://doi.org/10.1533/9780857091413.1.66.

[10] Kubásek, J. & Vojtěch, D. (2013). Structural characteristics and corrosion behavior of biodegradable Mg–Zn, Mg–Zn–Gd alloys. *Journal of Materials Science: Materials in*

Medicine. 24, 1615-1626. https://doi.org/10.1007/s10856-013-4916-3.

[11] Zberg, B., Uggowitzer, P.J. & Löffler, J.F. (2009). MgZnCa glasses without clinically observable hydrogen evolution for biodegradable implants. *Nature Materials.* 8(11), 887-891. https://doi.org/10.1038/nmat2542.

[12] Scully, J.R., Gebert, A. & Payer, J.H. (2007). Corrosion and related mechanical properties of bulk metallic glasses. *Journal of Materials Research.* 22(2), 302-313. https://doi.org/10.1557/jmr.2007.0051.

[13] Song, G., Atrens, A. & St John, D. (2001). An hydrogen evolution method for the estimation of the corrosion rate of magnesium alloys. In J. N. Hryn (Eds.), *Magnesium Technology.* https://doi.org/10.1002/9781118805497.ch44.

[14] Song, G.L. & Atrens, A. (1999). Corrosion mechanisms of magnesium alloys. *Advanced Engineering Materials.* 1(1), 11-33. https://doi.org/10.1002/(SICI)1527-2648(199909)1:1<11::AID-ADEM11>3.0.CO;2-N.

[15] Song, G. & Atrens, A. (2003). Understanding magnesium corrosion—a framework for improved alloy performance. *Advanced Engineering Materials.* 5(12), 837-858. https://doi.org/10.1002/adem.200310405.

[16] Inoue Akihisa. (1998). *Bulk amorphous alloys : preparation and fundamental characteristics.* Uetikon-Zuerich, Switzerland; Enfield, N.H.: Trans Tech Publications.

[17] Johnson, W.L. (1999). Bulk Glass-Forming Metallic Alloys: Science and Technology. *MRS Bulletin.* 24(10), 42-56. https://doi.org/10.1557/S0883769400053252.

[18] Löffler, J.F. (2003). Bulk metallic glasses. *Intermetallics.* 11(6), 529-540. https://doi.org/10.1016/S0966-9795(03)00046-3.

[19] Greer, A.L., Ma, E. (2007). Bulk metallic glasses: at the cutting edge of metals research. *MRS Bulletin.* 32(8), 611-619. https://doi.org/10.1557/mrs2007.121.

[20] Cao, J.D., Kirkland, N.T., Laws, K.J. et al. (2012). Ca–Mg–Zn bulk metallic glasses as bioresorbable metals. *Acta Biomaterialia.* 8(6), 2375-2383. https://doi.org/10.1016/j.actbio.2012.03.009.

[21] Gu, X., Shiflet, G.J., Guo, F.Q. & Poon, S.J. (2005). Mg–Ca–Zn bulk metallic glasses with high strength and significant ductility. *Journal of Materials Research.* 20, 1935-1938. https://doi.org/10.1557/JMR.2005.0245.

[22] Jang, J.S.C., Tseng, C.C., Chang, L.J., Chang, C.F. Lee, W.J. Huang, J.C. & Liu C.T. (2007). Glass forming ability and thermal properties of the Mg-based amorphous alloys with dual rare earth elements addition. *Materials Transactions.* 48(7), 1684-1688. https://doi.org/10.2320/matertrans.MJ200738.

[23] Qin, W., Li, J., Kou, H., Gu, X., Xue, X. & Zhou, L. (2009). Effects of alloy addition on the improvement of glass forming ability and plasticity of Mg–Cu–Tb bulk metallic glass. *Intermetallics.* 17(4), 253-255. https://doi.org/10.1016/j.intermet.2008.08.011.

[24] Park, E.S., Kyeong, J.S. & Kim, D.H. (2007). Enhanced glass forming ability and plasticity in Mg-based bulk metallic glasses. *Materials Science and Engineering A.* 449-451, 225-229. https://doi.org/10.1016/j.msea.2006.03.142.

[25] Lasia, A. (2002). Electrochemical impedance spectroscopy and its applications. In B.E. Conway, J. O'M. Bockris & R.E. White (Eds.), *Modern aspects of electrochemistry* (pp. 143-248). Boston, MA: Springer US.

[26] Liu, Y., Cao, H., Chen, S. & Wang, D. (2015). Ag nanoparticle-loaded hierarchical superamphiphobic surface on an al substrate with enhanced anticorrosion and antibacterial properties. *The Journal of Physical Chemistry C.* 119(45), 25449-25456. https://doi.org/10.1021/acs.jpcc.5b08679.